Article

Chiral assemblies of pinwheel superlattices on substrates

https://doi.org/10.1038/s41586-022-05384-8

Received: 30 April 2022

Accepted: 23 September 2022

Published online: 28 November 2022

Check for updates

Shan Zhou[1,2,13], Jiahui Li[1,13], Jun Lu[3,4,13], Haihua Liu[5], Ji-Young Kim[3,4], Ahyoung Kim[1], Lehan Yao[1], Chang Liu[1], Chang Qian[1], Zachary D. Hood[6], Xiaoying Lin[1,2], Wenxiang Chen[1,2], Thomas E. Gage[5], Ilke Arslan[5], Alex Travesset[7,8], Kai Sun[9], Nicholas A. Kotov[3,4,10] ✉ & Qian Chen[1,2,11,12] ✉

The unique topology and physics of chiral superlattices make their self-assembly from nanoparticles highly sought after yet challenging in regard to (meta)materials[1–3]. Here we show that tetrahedral gold nanoparticles can transform from a perovskite-like, low-density phase with corner-to-corner connections into pinwheel assemblies with corner-to-edge connections and denser packing. Whereas corner-sharing assemblies are achiral, pinwheel superlattices become strongly mirror asymmetric on solid substrates as demonstrated by chirality measures. Liquid-phase transmission electron microscopy and computational models show that van der Waals and electrostatic interactions between nanoparticles control thermodynamic equilibrium. Variable corner-to-edge connections among tetrahedra enable fine-tuning of chirality. The domains of the bilayer superlattices show strong chiroptical activity as identified by photon-induced near-field electron microscopy and finite-difference time-domain simulations. The simplicity and versatility of substrate-supported chiral superlattices facilitate the manufacture of metastructured coatings with unusual optical, mechanical and electronic characteristics.

Superlattices self-assembled from nanoparticles (NPs) have attracted extensive research attention due to their versatile composition and packing-dependent optical, magnetic, electronic, catalytic and mechanical properties[1–6]. Although they have been made from a variety of semiconductor, metal and ceramic materials showing a wide range of packing motifs, the experimental assembly of chiral NP superlattices remains fundamentally difficult[7,8] as can be reflected by the structural complexity associated with chirality[9]. Imparting chirality to NP superlattices and their thin films is needed for technological advances in (meta)surfaces because of the unique mechanical deformations and optical effects possible in chiral nanoassemblies[10,11]. Spontaneous thermodynamics-driven self-assembly of NPs can be associated with prohibitively high activation barriers because constituent particles have to overcome strong enthalpic and entropic preferences to form closely packed phases with lower levels of complexity. Simultaneously, this methodology will require NPs with exceptional uniformity and high asymmetry and thus new methods of enantioselective synthesis vastly different from previous approaches[12,13]. The strong face-to-face attraction between NPs also favours closely packed achiral superlattices[7,8,14]. Templated assemblies are capable of circumventing this challenge by assembling achiral NPs with biomolecular ligands on helical scaffolds that have proved effective for translation of chirality into clusters of a few particles[15,16], but not into large arrays; NPs connected by biological ligands produced colloidal crystals with achiral packings[17,18].

Learning from condensed matter physics, it should be possible to self-assemble open chiral superlattices from NPs by transforming non-closely packed achiral corner-sharing structures into new states with higher packing fraction by reconfiguring building blocks with tetrahedral and other polyhedral geometries (Fig. 1). No chirality of the constitutive particles is needed—in fact, numerous achiral ones can be utilized. Prominent examples of corner-sharing materials (Fig. 1a) include perovskite, pyrochlore, diamond and zeolite, which are widely explored in regard to imparting ferroelectricity, piezoelectricity, superconductivity, spin filtering, optical activity and other properties to different materials[19,20]. In these materials, symmetry-breaking phase transitions can be driven by changes in pressure, stoichiometry, temperature or the surface chemistry of the building blocks[21–25].

The same geometrical advantages that make the assembly of open chiral superlattices from tetrahedral building blocks attractive, however, also hinder their experimental realization. It is well known that tetrahedra can produce singular helices or quasi-crystals, but self-assembly into regular periodic superlattices encounters a large

[1]Department of Materials Science and Engineering, University of Illinois at Urbana-Champaign, Urbana, IL, USA. [2]Materials Research Laboratory, University of Illinois at Urbana-Champaign, Urbana, IL, USA. [3]Department of Chemical Engineering, University of Michigan, Ann Arbor, MI, USA. [4]Biointerfaces Institute, University of Michigan, Ann Arbor, MI, USA. [5]Center for Nanoscale Materials, Argonne National Laboratory, Lemont, IL, USA. [6]Applied Materials Division, Argonne National Laboratory, Lemont, IL, USA. [7]Department of Physics and Astronomy, Iowa State University and Ames Lab, Ames, IA, USA. [8]Department of Materials Science and Engineering, Iowa State University and Ames Lab, Ames, IA, USA. [9]Department of Physics, University of Michigan, Ann Arbor, MI, USA. [10]Department of Materials Science and Engineering, University of Michigan, Ann Arbor, MI, USA. [11]Beckman Institute for Advanced Science and Technology, University of Illinois at Urbana-Champaign, Urbana, IL, USA. [12]Department of Chemistry, University of Illinois at Urbana-Champaign, Urbana, IL, USA. [13]These authors contributed equally: Shan Zhou, Jiahui Li, Jun Lu. ✉e-mail: kotov@umich.edu; qchen20@illinois.edu

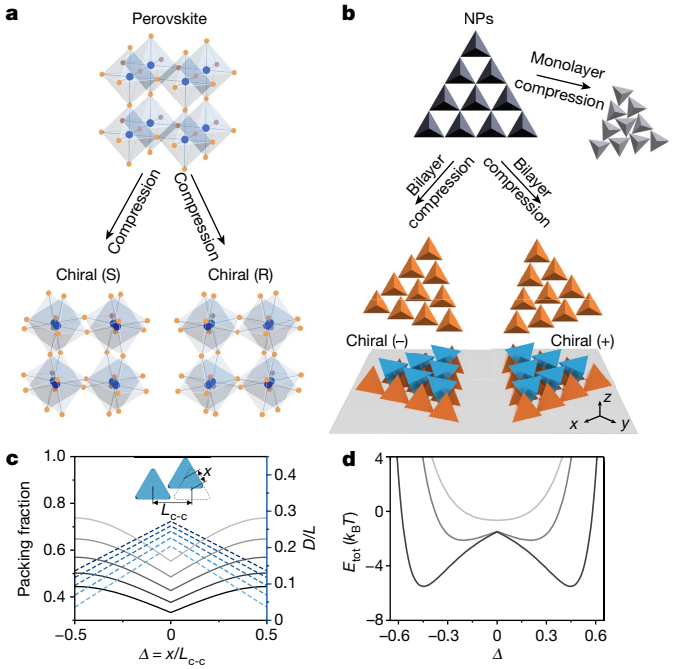

Fig. 1 | Chiral symmetry breaking in superlattices from tetrahedra undergoing phase transition from low- to high-packing fraction states. **a**, Schematics showing the transformation of non-closely packed achiral corner-sharing perovskite-like lattice into chiral states with a higher packing fraction[21]. Crystal structures are modified from chiral perovskites S-3AP–NH_4Br_3 and R-3AP–NH_4Br_3. **b**, Schematics for chiral symmetry breaking of achiral corner-sharing bilayer lattice into pinwheel lattice on substrates. During twisting, corner-to-corner connections originating from physical interactions switch seamlessly to corner-to-edge connections rather than the corner-to-corner chemical bonds constrained in atomic crystals. **c**, Packing fraction (left *y* axis) and *D* change (right *y* axis) as a function of corner offset Δ, defined as the ratio of travel distance *x* and initial centre-to-centre distance $L_{c\text{-}c}$ in corner-to-corner alignment. Gradation of line colour from dark to light represents change in the ratio of tetrahedron truncation (defined in Supplementary Note 1) from 0 to 0.16. **d**, Energy diagram showing interparticle interaction as a function of Δ. Gradation of line colour from light to dark represents the energy diagram for small, medium- and large-sized tetrahedra, respectively. Calculations in **d** used geometric parameters obtained from the experimental results (Supplementary Tables 3 and 4).

number of kinetically arrested states[7,8,26,27]. Here we show how the set of multifaceted difficulties mentioned above is overcome, starting from a robust method to synthesize and purify gold tetrahedral NPs with tuneable edge length *L* ranging from 30 to 100 nm and with low dispersity (4.8–8.7%) (Fig. 2a, Methods, Supplementary Figs. 1 and 2 and Supplementary Table 1). Compared with previous studies on tetrahedral semiconductor NPs that assemble face to face[7,8,26], gold tetrahedra are mostly coated by positively charged cetyltrimethylammonium bromide (CTAB) ligands with corners stabilized by thiols (Supplementary Fig. 3 and Supplementary Table 2), which increases face-to-face repulsion.

Controlled evaporation of an aqueous solution of nanoscale gold tetrahedra on a Si wafer drives their assembly into non-trivial bilayer lattices composed of two interlacing sets of corner-sharing tetrahedra (Figs. 1b and 2a–d and Methods). It has a low-packing fraction of 1/3 (Fig. 1c), lower than that of all predicted assembly structures of tetrahedra[28] (Supplementary Fig. 4 and Supplementary Note 1). As shown in Fig. 2d, the bottom-layer tetrahedra sit on the Si substrate with corners pointing upwards (orange triangles) and top-layer tetrahedra fill the triangular voids with corners pointing downwards (blue triangles). Fast Fourier transform (FFT) of the scanning electron microscopy (SEM) image shows a pattern resembling a honeycomb structure (Fig. 2d). The unit cell of the bilayer lattice shows a pair of neighbouring tetrahedral NPs facing in opposite directions along the *z* axis (Fig. 2b). Particle tracking measures a large face-to-face distance, *D*, of 11.2 nm between this NP pair (Fig. 2c, Supplementary Figs. 5–7 and Supplementary Notes 1 and 2); even considering the thickness of adsorbed CTAB ligands (3.2 nm on each tetrahedron)[29], this NP pair is not physically in contact at the faces (Fig. 2c and Supplementary Table 3). Our coarse-grained modelling of the total pairwise interparticle interaction shows that the achiral bilayer lattice with nearly perfect corner-to-corner connection is favoured for small-sized gold tetrahedra of 32.1 nm at an ionic strength, *I*, of 30 mM (Fig. 1d and Supplementary Note 3) by balancing van der Waals attraction (E_{vdW}) between tetrahedra and electrostatic repulsion (E_{el}) between charged ligands, which can be achieved in the solution during the drying process. The face-to-face repulsion (0.59 k_BT; Supplementary Note 3) separates the faces of tetrahedra, allowing only corner-to-corner connections, leading to this previously inaccessible low-packing fraction lattice. Although the inspiration is derived from atomic systems, the linkages of corner-sharing structures are not permeant chemical bonds but physical colloidal interactions, which allow for different compression pathways and potentially rich design space.

Pinwheel lattices with corner-to-edge connections and greater packing fractions are achieved when a spontaneous in-plane 'compression' is induced by weakening E_{el} and/or increasing E_{vdW}. For example, large tetrahedra (L = 68.6 nm) increase E_{vdW} and, hence, form extended domains (over 35 μm^2; Supplementary Fig. 8) of pinwheel packing (Fig. 2e) with corner-to-edge connections, in which decreased *D* and increased packing fraction are observed (Fig. 1c). This twisted pinwheel structure is predicted by neither existing theory nor simulations[27,28,30–32] and is different from what has been experimentally realized previously[7,8,33]. Note that only in the bilayer superlattice do all tetrahedra slide in the same direction and to the same degree, due to the equilateral constraints imposed by the top layer of tetrahedra, which would not be the case for a monolayer of tetrahedral particles (Fig. 1b and Supplementary Video 1). The corresponding FFT pattern exhibits a consistent twist over a hexagonal pattern characteristic of the original achiral lattice (Fig. 2e). The effective 'compression' increases the packing fraction to 4/9 when all tetrahedra rotate in-plane by 30° (Fig. 1b,c, Supplementary Note 1 and Supplementary Fig. 7) and changes the point group from D_{3d} to S_6 (Fig. 2c and Supplementary Video 1). Graph theoretical (GT) representations of the honeycomb and pinwheel superlattices reveal an increasing functional complexity index (*CI*) of these nanoassemblies from 27 to 29 (Supplementary Note 4 and Supplementary Fig. 9a,b). This increase is associated with the opening of the intralattice cavities with GT representation as a simple loop graph, while their functionality becomes obvious from the emergence of chiroptical properties.

We note that free-standing pinwheel superlattices of the corner-to-edge assemblies of tetrahedra are inversion symmetric but become chiral when deposited on a flat substrate, similar to early reports on top-down fabricated quasi-planar nanostructures and limited-sized NP assemblies[34,35]. The pinwheels can be superimposed onto their mirror image if flipping in the *z* direction is allowed. When the substrate is present, flipping of the structure will, however, lead to positional change of the substrate that leads to an inequivalent mirror image of the original structure (Supplementary Fig. 7 and Supplementary Video 2). This effect can be demonstrated by calculating the chirality measure with the Osipov–Pickup–Dunmur parameter[36,37] (OPD) of a free-standing pinwheel lattice in the absence of a substrate (OPD = 0) (Supplementary Fig. 9, Supplementary Note 4 and Supplementary Table 5), which becomes either positive or negative indicating the assembly of opposite chirality with inclusion of a substrate (Fig. 3a, Supplementary Fig. 10 and Supplementary Table 6). This substrate effect is captured in the OPD calculation by considering not only the centre of mass (CoM) position of each tetrahedron, but also those of corners and substrate

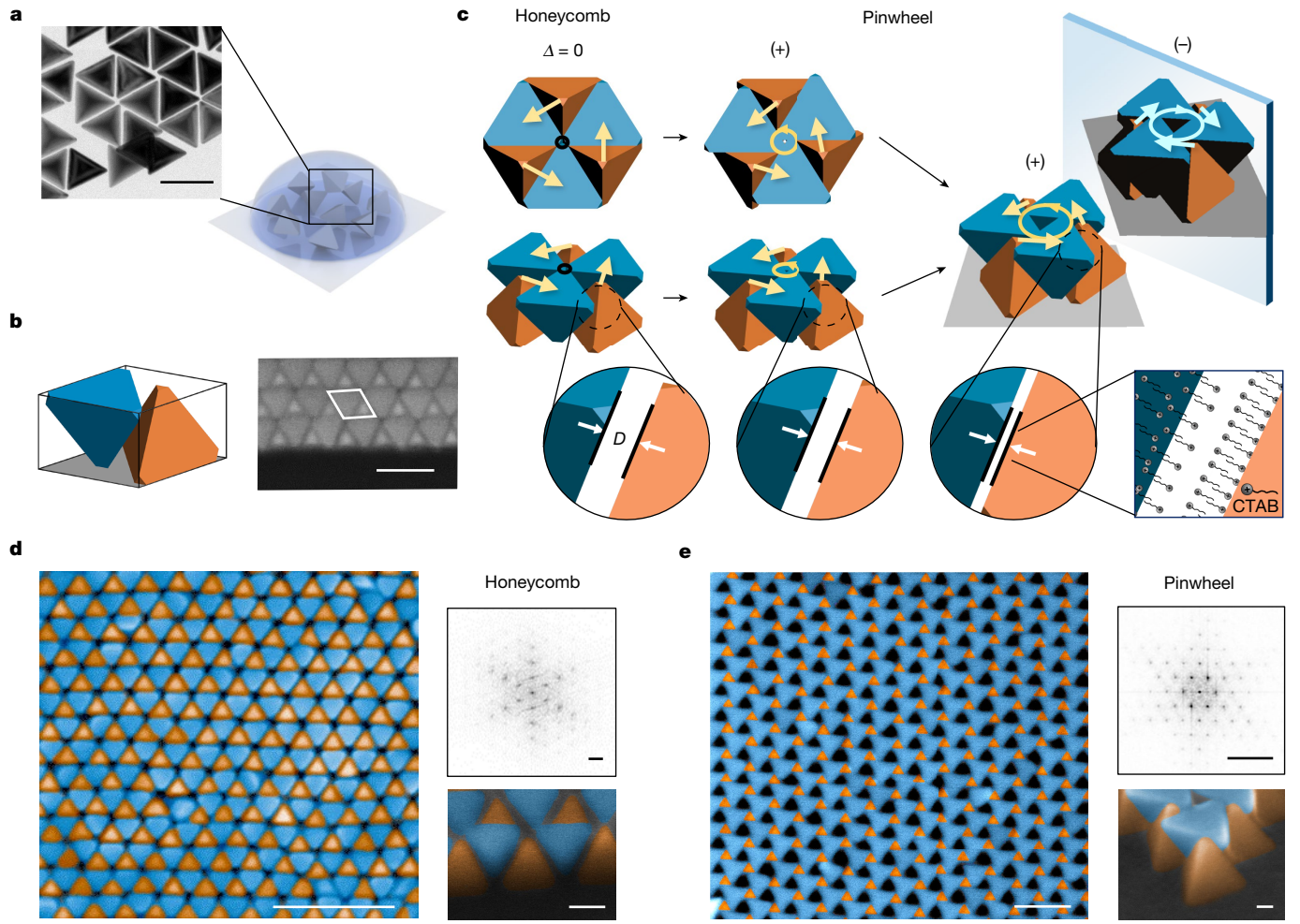

Fig. 2 | Corner-sharing and pinwheel bilayer superlattices with corner-to-edge connections from gold tetrahedral NPs. a, Schematic of the evaporation-driven self-assembly on a Si wafer and TEM image of gold tetrahedral building blocks. **b**, Schematic of the bilayer unit cell and SEM image, showing the boundary of a corner-sharing bilayer domain. The white box in the SEM image showing the unit cell serves as a visual guide. **c**, Schematics of the transition from corner-sharing tetrahedron bilayer lattice to pinwheel lattice. The twisting of tetrahedra in-plane is accompanied by decreasing face-to-face distance D for interlayer neighbouring tetrahedra, as shown in the zoomed-in schematics. Tetrahedra are coated by positively charged CTAB, as shown in the zoom-in schematics. **d**,**e**, SEM images (left), FFT (top right) and tilted SEM images (bottom right) of the large-scale extended corner-sharing lattice (**d**) and pinwheel lattice (**e**) formed by tetrahedral building blocks on substrates. Precise assembly conditions can be found in Supplementary Table 2. Scale bars: **a**,**b**, 100 nm; **d**,**e**, 200 nm (top view), 20 nm (tilted view) and 10 nm^{-1} (FFT).

(Supplementary Note 4). |OPD| of the total structure changes from 0 to a higher value when the corner offset (Δ; see definition in Fig. 1c and Supplementary Note 2), a physical measurement of symmetry breaking, increases (Fig. 3a and Supplementary Table 6). Experimentally the pinwheel superlattices must always sit on the substrate, making the domains with opposite handedness true enantiomers. Incident polarized light thus distinguishes the top and bottom tetrahedra and undergoes polarization rotation, making the pinwheels chiroptically active. This chirality can be enumerated by the corner offset Δ. Variation in NP size, ionic strength and molecular additives results in systematic changes of $|\Delta|$ from 0.03 to 0.56 (Supplementary Figs. 5 and 6 and Supplementary Table 4). Correspondingly, |OPD| for the lattices on the substrate changes roughly from 0 to 1.68. In the experiment, we differentiate the corner-sharing honeycomb lattice and corner-to-edge pinwheel lattice using a threshold $|\Delta|$ of 0.05 (Supplementary Table 4).

The structure-dependent chiroptical properties of these superlattices are demonstrated by their optical activity measured using photon-induced near-field electron microscopy (PINEM)[38–40] in an ultrafast electron microscope (UEM) (Fig. 3 and Supplementary Figs. 11–19). PINEM maps plasmonic fields near the nanostructures by selecting electrons that gain energy due to photon–electron interactions when electrons overlap photons spatiotemporally near the nanostructures (Fig. 3b). This method has been used for studies of achiral nanostructures[41], but it can also be used for chiral nanostructures when the traditional macroscale circular dichroism (CD) spectroscopy is inapplicable. We use left-handed (LCP) and right-handed circularly polarized (RCP) light to excite plasmonic fields and monitor chiral response. Compared with state-of-the-art methods of single-particle CD or polarized light optical microscopy[42], PINEM directly measures the electric field (E-field) distributions of nanostructures at nanometre spatial resolution (that is, two orders of magnitude higher).

Pump laser pulses of 50 fs duration with LCP or RCP light illuminate the pinwheel assemblies with varying Δ, handedness and domain size (Fig. 3b). For chiral pinwheel lattices, E-field distributions have apparent differences under irradiation by LCP and RCP (Fig. 3b–f and Supplementary Figs. 11 and 12). With the four-particle domain of $\Delta = -0.2$ as an example, strong plasmonic resonance in the E-field is located at the right corner under LCP in comparison with that located at the top corner under RCP (Fig. 3b), consistent with the E-field maps obtained from finite-difference time-domain (FDTD) simulation

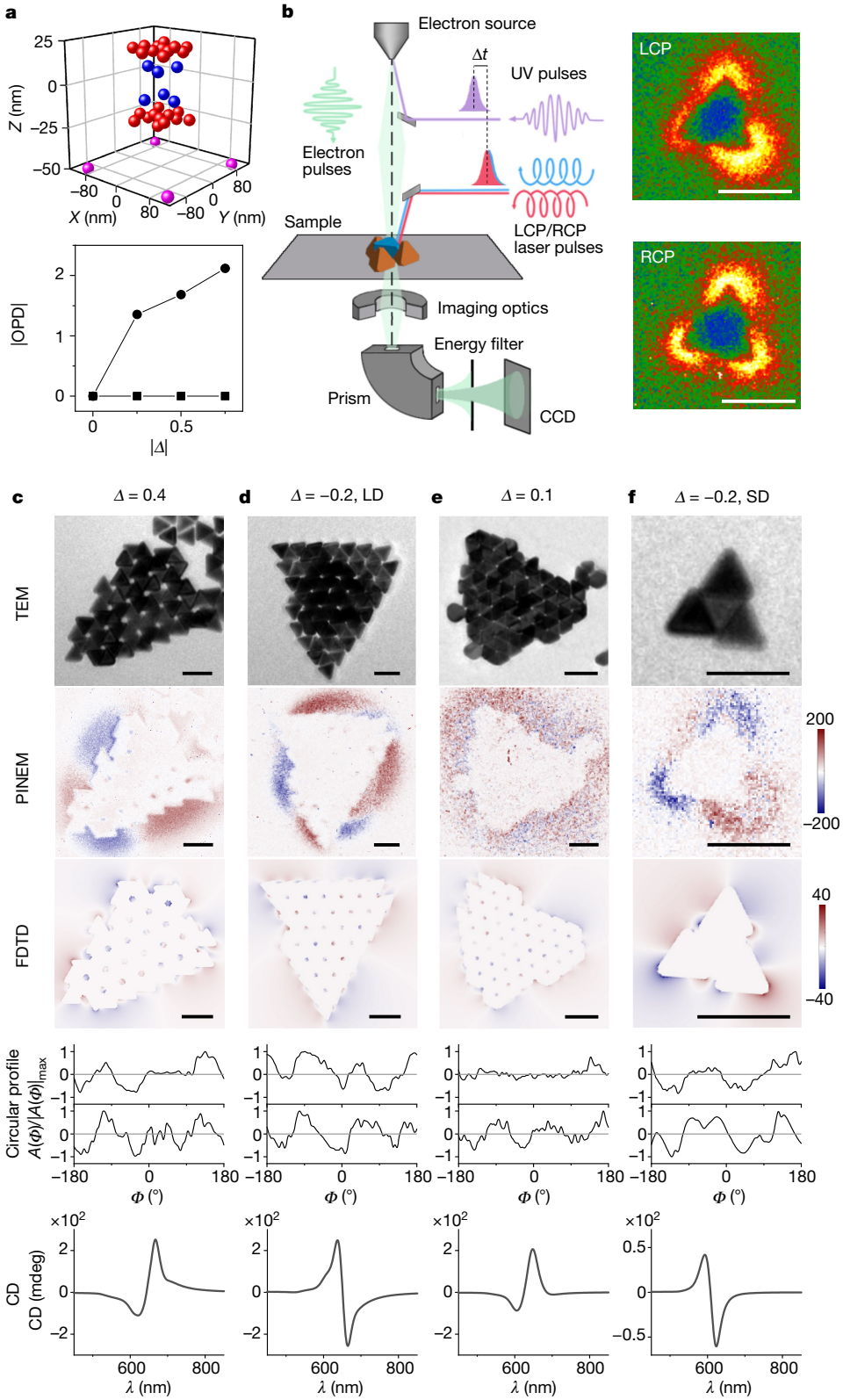

Fig. 3 | Chirality of pinwheel bilayer lattices deposited on solid substrates. **a**, OPD chirality measures calculated from extracted point groups in Cartesian coordinate system (top) for varying Δ (bottom) with (circular markers) and without (square markers) considering the substrate. The point coordinates are extracted from corners (red dots) and CoMs (blue dots) of the pinwheel lattice with $\Delta = 0.5$ and the substrate (magenta dots). **b**, Schematic of the PINEM set-up for single-NP-level chiroptical activity characterization. LCP or RCP laser pulses are applied as the excitation light source and photo-excite the plasmonic field. CCD, charge-coupled device. **c**–**f**, TEM images, PINEM subtracted *E*-field maps of LCP–RCP, FDTD-simulated subtracted *E*-field distribution, normalized circular profiles and CD spectra (from top to bottom) of chiral pinwheel bilayer lattices on TEM grids of varying domain size, as well as magnitudes and signs of Δ (**c**, 0.4; **d**, −0.2, LD; **e**, 0.1; **f**, −0.2, SD). The excitation wavelength $\lambda = 670$ nm is used in both PINEM measurements and FDTD simulations. SD, small domain; LD, large domain. Laser fluence is 0.8 mJ cm^{-2} (**c**,**d**,**f**) or 1.2 mJ cm^{-2} (**e**). Normalized circular profiles are calculated based on *E*-field intensity, *A*, as a function of rotation angle Φ and normalized by the absolute maximum *E*-field intensity $|A(\Phi)|_{max}$ for PINEM (top) and FDTD (bottom) subtracted maps. Scale bars, 100 nm.

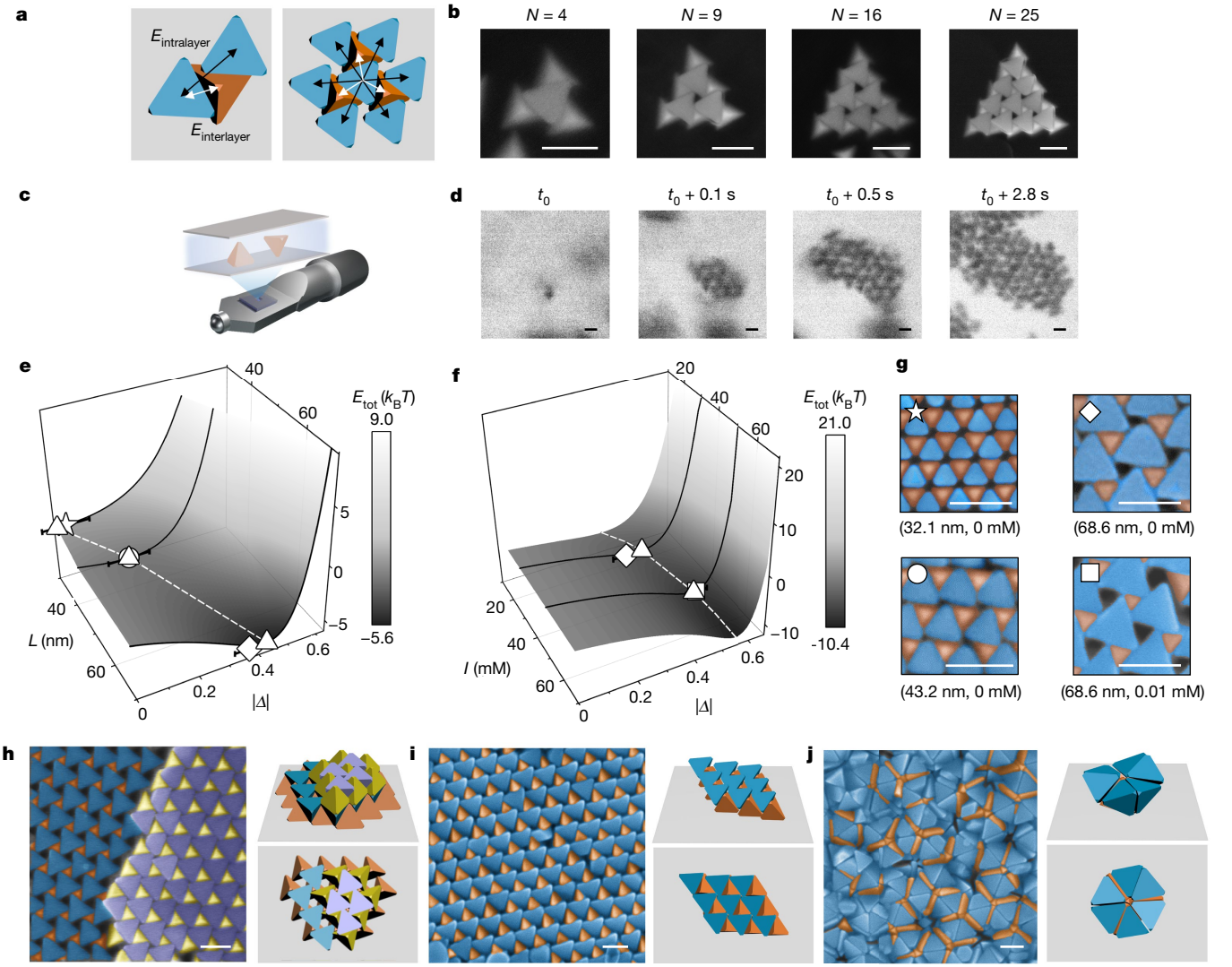

Fig. 4 | Formation mechanism and controllability of self-assembled chiral superlattices from tetrahedral NPs. a, Models for interaction calculations considering one interlayer and two intralayer interactions as the representative motifs for the chiral pinwheel lattice. **b**, SEM images of small bilayer domains formed at a lower particle concentration (Supplementary Table 2). **c**,**d**, Schematic (**c**) and snapshots (**d**) of in situ nucleation and growth process of bilayer lattice using liquid-phase TEM. **e**, Three-dimensional (3D) energy diagram showing interparticle interaction as a function of Δ and L. **f**, 3D energy diagram showing interparticle interaction as a function of Δ and ionic strength I. The range of I in the calculation is higher than the initial salt concentration in experiments, due to increased salt concentration during evaporation. Star, circle, diamond and square markers with error bars indicate the experimental Δ and corresponding standard deviations of the assembled structures shown in **g**, and triangles indicate the positions of energy minima in the calculation given the same L or I. n = 850 for star marker, n = 616 for circle and diamond markers, n = 1,868 for square marker. **g**, SEM images of chiral bilayers assembled on a substrate with differently sized tetrahedra and different initial salt concentration c_{NaCl}, denoted by L, c_{NaCl}. **h**–**j**, SEM images and schematics of tetrahedral assembly driven by stronger interparticle attractions: multilayer with z-direction protrusion (**h**), tilted assembly without three-fold rotational symmetry (**i**) and face-to-face packing (**j**). Precise assembly conditions and lattice parameters can be found in Supplementary Tables 2–4. Scale bars, 100 nm.

(Supplementary Figs. 13 and 14). Optical asymmetry can be further highlighted by subtraction of E-field maps under LCP and RCP (Fig. 3b, Supplementary Fig. 12 and Supplementary Note 5) with outcomes matching nearly perfectly the FDTD simulations (Supplementary Figs. 13–15). The calculated CD spectra exhibit red-shifts of peaks and increase in intensity with increase in domain size (number of NPs per domain, N = 4–73) (Fig. 3d,f), indicating strong optical asymmetry for these metamaterials. We have also verified that the chirality of the pinwheel lattice does not originate from the potential generic chirality of the tetrahedral building blocks due to uneven corner truncations or heterogeneous distributions of surface ligands (Supplementary Figs. 1, 2 and 17 and Supplementary Note 5).

At similar domain sizes, chiroptical activity shows a clear dependency on Δ (Fig. 3c–e). For the domain with Δ = 0, the subtracted E-field has a weak and alternative localized pattern corresponding to the near-zero signal in the CD spectra (Supplementary Fig. 16). For the domain with limited Δ = 0.1, the subtracted E-field distribution becomes diffusive around the domain in experiments and shows a similar weak chiral localized feature and low CD peak in the simulation (Fig. 3e). For domains with a large $|\Delta|$ = 0.2–0.4, the subtracted E-field distribution adopts a pattern with clearly asymmetrical localized and alternative signals with opposite signs outside the domain (Fig. 3c,d). The normalized circular profile for the domain with higher $|\Delta|$ shows more distinct features (Fig. 3c–e), which also matches the appearance of greater

amplitude in the calculated CD spectra (Supplementary Figs. 17 and 18). The domains with opposite handedness exhibit reversed peaks in CD responses (Fig. 3c,d), indicating that the pinwheel lattice is truly mirror-asymmetric on the substrate.

The structural dependence of chiroptical activity enables tuneable symmetry breaking. Our control evaporation experiments at low particle concentrations (Fig. 4a,b and Supplementary Fig. 20a) point to the mechanism by which individual tetrahedral NPs first assemble into $N = 4$ pinwheel (the smallest to adopt chirality), which grows into extended domains with identical handedness. This process is corroborated by liquid-phase transmission electron microscopy (TEM) experiments[43–46] (Fig. 4c, Methods and Supplementary Note 6), where individual tetrahedral NPs are observed to assemble and extend into a bilayer lattice within seconds (Fig. 4d and Supplementary Fig. 20b) following an increase in ionic strength, I. Thus, we find that the sum of one interlayer and two intralayer interactions is able to predict the stable pinwheel structure, quantitatively matching the experiments (Supplementary Note 3, Supplementary Figs. 21–23 and Supplementary Table 7). The predicted energy minimum locates at increasing Δ (0–0.44) as particle L increases from 32.1 to 68.6 nm (Fig. 4e), consistent with our experimentally observed Δ increasing from 0.03 to 0.38 (Fig. 4g). The predicted total energy minimum also occurs at an increasing Δ of 0.44–0.52 when I increases from 30 to 50 mM (Fig. 4f and Supplementary Fig. 21), which we confirm experimentally when Δ of the final assembly changes from 0.38 to 0.53 as we increase initial NaCl concentration in the solution (Fig. 4g). As we further increase I to 'compress' the open superlattices, symmetry breaking can be extended into three dimensions (Fig. 4h,i). Multilayer structures (Supplementary Fig. 24) with corner protrusion in all the top bilayers (Fig. 4h) or tilted assemblies without three-fold symmetry (Fig. 4i) are formed, rendering them truly chiral even in the absence of substrate. These assemblies with variable offsets or tilts around the z axis can further decrease D and increase packing fraction. An even higher I leads to a complete collapse into dense face-to-face decahedral packing (Fig. 4j).

Conclusion

Previously unknown perovskite-like, corner-sharing superlattices with ultralow-packing density are self-assembled from nanoscale tetrahedra. The equilibrium configurations of the pinwheel structural motif in these superlattices can be controlled by attractive and repulsive interactions between NPs, leading to superlattices of variable chirality. Whereas the original corner-sharing nanoassemblies are achiral, the compacted superlattices with corner-to-edge connections become chiral when resting on solid substrates. Potential strategies to further push the handedness of our pinwheel lattice to one side could include chiral molecules[2] that provide a chiral bias to direct the packing order of NPs via coordination, electrostatic interaction and hydrogen bonding; and circularly polarized light[36] to adjust the asymmetric displacement of NPs under the asymmetrical electronic and magnetic fields from beam sources, which have proved effective for other gold NPs including gold nanorods and gold nanospheres. Our findings can be extended to a large library of achiral particles, their non-closely packed assemblies and lattice reconfiguration pathways, which also allow for rich design space of metastructured surfaces with substrate-induced chiroptical activity (Supplementary Fig. 25). Besides unique polarization rotation, these superlattices are expected to exhibit an emergent conformal symmetry (Supplementary Fig. 26) and zero-energy edge modes, in analogy to the twisted kagome lattice[47,48].

Online content

Any methods, additional references, Nature Portfolio reporting summaries, source data, extended data, supplementary information, acknowledgements, peer review information; details of author contributions and competing interests; and statements of data and code availability are available at https://doi.org/10.1038/s41586-022-05384-8.

1. Singh, G. et al. Self-assembly of magnetite nanocubes into helical superstructures. *Science* **345**, 1149–1153 (2014).
2. Lu, J. et al. Enhanced optical asymmetry in supramolecular chiroplasmonic assemblies with long-range order. *Science* **371**, 1368–1374 (2021).
3. Li, S. et al. Single- and multi-component chiral supraparticles as modular enantioselective catalysts. *Nat. Commun.* **10**, 4826 (2019).
4. Kotov, N. A., Meldrum, F. C., Wu, C. & Fendler, J. H. Monoparticulate layer and Langmuir–Blodgett-type multiparticulate layers of size-quantized cadmium sulfide clusters: a colloid-chemical approach to superlattice construction. *J. Phys. Chem.* **98**, 2735–2738 (1994).
5. Jeong, U., Teng, X., Wang, Y., Yang, H. & Xia, Y. Superparamagnetic colloids: controlled synthesis and niche applications. *Adv. Mater.* **19**, 33–60 (2007).
6. Xia, Y. et al. One-dimensional nanostructures: synthesis, characterization, and applications. *Adv. Mater.* **15**, 353–389 (2003).
7. Nagaoka, Y., Zhu, H., Eggert, D. & Chen, O. Single-component quasicrystalline nanocrystal superlattices through flexible polygon tiling rule. *Science* **362**, 1396–1400 (2018).
8. Nagaoka, Y. et al. Superstructures generated from truncated tetrahedral quantum dots. *Nature* **561**, 378–382 (2018).
9. Jiang, W. et al. Emergence of complexity in hierarchically organized chiral particles. *Science* **368**, 642–648 (2020).
10. Jenett, B. et al. Discretely assembled mechanical metamaterials. *Sci. Adv.* **6**, eabc9943 (2020).
11. Frenzel, T., Kadic, M. & Wegener, M. Three-dimensional mechanical metamaterials with a twist. *Science* **358**, 1072–1074 (2017).
12. Feringa, B. L. & Van Delden, R. A. Absolute asymmetric synthesis: the origin, control, and amplification of chirality. *Angew. Chem. Int. Ed. Engl.* **38**, 3418–3438 (1999).
13. Lelais, G. & MacMillan, D. W. Modern strategies in organic catalysis: the advent and development of iminium activation. *Aldrichimica Acta* **39**, 79–87 (2006).
14. Henzie, J., Grünwald, M., Widmer-Cooper, A., Geissler, P. L. & Yang, P. Self-assembly of uniform polyhedral silver nanocrystals into densest packings and exotic superlattices. *Nat. Mater.* **11**, 131–137 (2012).
15. Zhou, Y. et al. Biomimetic hierarchical assembly of helical supraparticles from chiral nanoparticles. *ACS Nano* **10**, 3248–3256 (2016).
16. Kuzyk, A. et al. DNA-based self-assembly of chiral plasmonic nanostructures with tailored optical response. *Nature* **483**, 311–314 (2012).
17. Samanta, D., Zhou, W., Ebrahimi, S. B., Petrosko, S. H. & Mirkin, C. A. Programmable matter: the nanoparticle atom and DNA bond. *Adv. Mater.* **34**, e2107875 (2022).
18. Nykypanchuk, D., Maye, M. M., Van Der Lelie, D. & Gang, O. DNA-guided crystallization of colloidal nanoparticles. *Nature* **451**, 549–552 (2008).
19. Fazileh, F., Chen, X., Gooding, R. J. & Tabunshchyk, K. Electronic properties of disordered corner-sharing tetrahedral lattices. *Phys. Rev. B* **73**, 035124 (2006).
20. Xu, X. & Wang, X. Perovskite nano-heterojunctions: synthesis, structures, properties, challenges, and prospects. *Small Struct.* **1**, 2000009 (2020).
21. Ye, H.-Y. et al. Metal-free three-dimensional perovskite ferroelectrics. *Science* **361**, 151–155 (2018).
22. He, J., Borisevich, A., Kalinin, S. V., Pennycook, S. J. & Pantelides, S. T. Control of octahedral tilts and magnetic properties of perovskite oxide heterostructures by substrate symmetry. *Phys. Rev. Lett.* **105**, 227203 (2010).
23. Lu, W. et al. The role of octahedral tilting in the structural phase transition and magnetic anisotropy in $SrRuO_3$ thin film. *J. Appl. Phys.* **113**, 063901 (2013).
24. Rondinelli, J. M., May, S. J. & Freeland, J. W. Control of octahedral connectivity in perovskite oxide heterostructures: an emerging route to multifunctional materials discovery. *MRS Bull.* **37**, 261–270 (2012).
25. Smith, P. F. et al. Coordination geometry and oxidation state requirements of corner-sharing MnO_6 octahedra for water oxidation catalysis: an investigation of manganite (γ-MnOOH). *ACS Catal.* **6**, 2089–2099 (2016).
26. Haji-Akbari, A. et al. Disordered, quasicrystalline and crystalline phases of densely packed tetrahedra. *Nature* **462**, 773–777 (2009).
27. Serafin, F., Lu, J., Kotov, N., Sun, K. & Mao, X. Frustrated self-assembly of non-Euclidean crystals of nanoparticles. *Nat. Commun.* **12**, 4925 (2021).
28. Conway, J. H. & Torquato, S. Packing, tiling, and covering with tetrahedra. *Proc. Natl Acad. Sci. USA* **103**, 10612–10617 (2006).
29. Gómez-Graña, S. et al. Surfactant (bi)layers on gold nanorods. *Langmuir* **28**, 1453–1459 (2012).
30. Damasceno, P. F., Engel, M. & Glotzer, S. C. Crystalline assemblies and densest packings of a family of truncated tetrahedra and the role of directional entropic forces. *ACS Nano* **6**, 609–614 (2012).
31. Haji-Akbari, A., Engel, M. & Glotzer, S. C. Phase diagram of hard tetrahedra. *J. Chem. Phys.* **135**, 194101 (2011).
32. Jin, W., Lu, P. & Li, S. Evolution of the dense packings of spherotetrahedral particles: from ideal tetrahedra to spheres. *Sci Rep.* **5**, 15640 (2015).
33. Boles, M. A. & Talapin, D. V. Self-assembly of tetrahedral CdSe nanocrystals: effective "patchiness" via anisotropic steric interaction. *J. Am. Chem. Soc.* **136**, 5868–5871 (2014).
34. Kuwata-Gonokami, M. et al. Giant optical activity in quasi-two-dimensional planar nanostructures. *Phys. Rev. Lett.* **95**, 227401 (2005).
35. Nechayev, S., Barczyk, R., Mick, U. & Banzer, P. Substrate-induced chirality in an individual nanostructure. *ACS Photonics* **6**, 1876–1881 (2019).
36. Kim, J.-Y. et al. Assembly of gold nanoparticles into chiral superstructures driven by circularly polarized light. *J. Am. Chem. Soc.* **141**, 11739–11744 (2019).
37. Osipov, M. A., Pickup, B. T. & Dunmur, D. A. A new twist to molecular chirality: intrinsic chirality indices. *Mol. Phys.* **84**, 1193–1206 (1995).
38. Feist, A. et al. Quantum coherent optical phase modulation in an ultrafast transmission electron microscope. *Nature* **521**, 200–203 (2015).

39. Barwick, B., Flannigan, D. J. & Zewail, A. H. Photon-induced near-field electron microscopy. *Nature* **462**, 902–906 (2009).
40. Piazza, L. et al. Simultaneous observation of the quantization and the interference pattern of a plasmonic near-field. *Nat. Commun.* **6**, 6407 (2015).
41. Liu, H. et al. Visualization of plasmonic couplings using ultrafast electron microscopy. *Nano Lett.* **21**, 5842–5849 (2021).
42. Vinegrad, E. et al. Circular dichroism of single particles. *ACS Photonics* **5**, 2151–2159 (2018).
43. Zhu, G. et al. Self-similar mesocrystals form via interface-driven nucleation and assembly. *Nature* **590**, 416–422 (2021).
44. Kim, B. H. et al. Critical differences in 3D atomic structure of individual ligand-protected nanocrystals in solution. *Science* **368**, 60–67 (2020).
45. Ou, Z., Wang, Z., Luo, B., Luijten, E. & Chen, Q. Kinetic pathways of crystallization at the nanoscale. *Nat. Mater.* **19**, 450–455 (2020).
46. Liu, C. et al. "Colloid–atom duality" in the assembly dynamics of concave gold nanoarrows. *J. Am. Chem. Soc.* **142**, 11669–11673 (2020).
47. Sun, K., Souslov, A., Mao, X. & Lubensky, T. Surface phonons, elastic response, and conformal invariance in twisted kagome lattices. *Proc. Natl Acad. Sci. USA* **109**, 12369–12374 (2012).
48. Mao, X. & Lubensky, T. C. Maxwell lattices and topological mechanics. *Annu. Rev. Condens. Matter Phys.* **9**, 413–433 (2018).

Methods

Chemicals

Gold(III) chloride trihydrate (49.0% or over, $HAuCl_4 \cdot 3H_2O$; Sigma-Aldrich), cetyltrimethylammonium chloride (CTAC) (25 wt% in H_2O and $CH_3(CH_2)_{15}N(Cl)(CH_3)_3$; Sigma-Aldrich), L-ascorbic acid (AA) (BioXtra, 99.0% or over; Sigma-Aldrich), Rhodamine 6G (approximately 95%, Sigma-Aldrich), sodium chloride (99.0% or above, NaCl; Fisher Chemical), sodium phosphate dibasic anhydrous (over 99%, Na_2HPO_4; Acros), 2-(2-[2-(11-mercapto-undecyloxy)-ethoxy]-ethoxy)-ethoxy-ethoxy-ethoxy-acetic acid (95% or above, $HS(CH_2)_{11}(OC_2H_4)_6OCH_2COOH$; Prochimia Surfaces), sodium phosphate monobasic monohydrate (99.0–102.0%, $NaH_2PO_4 \cdot H_2O$; EMD Millipore), CTAB (99.0% or over; BioXtra, $CH_3(CH_2)_{15}N(Br)(CH_3)_3$; Sigma-Aldrich), sodium borohydride ($NaBH_4$, 98 %), acetone (99.5% or over; Fisher Chemical) and isopropanol (99.9%; Fisher Chemical) were purchased and used without further purification. Water used in this work was nanopure water (18.2 MΩ cm at 25 °C) purified by the Milli-Q Advantage A10 system.

Synthesis of gold tetrahedra

The gold tetrahedra used here were synthesized following a method previously described, with slight modification[49]. Freshly prepared aqueous solutions of $HAuCl_4$ (63.5 µl, 40 mM) and CTAB (9.94 ml, 100 mM) were mixed in a 20 ml scintillation vial by shaking at 400 rpm for 2 min. A fresh aqueous $NaBH_4$ solution (10 mM, 0.6 ml) was then rapidly added to the vial by pipette. The reaction mixture rapidly changed in colour from light yellow to brown. The mixture was placed on an orbital shaker at a speed of 400 rpm for 2 min, then left undisturbed at room temperature for 5 h to ensure complete decomposition of $NaBH_4$. In the second step[50], aqueous solutions of $HAuCl_4$ (0.5 mM, 2 ml), CTAC (200 mM, 2 ml) and AA (100 mM, 1.5 ml) were sequentially added to a 20 ml scintillation vial and the solution thoroughly mixed by shaking at 400 rpm for 2 min with each addition. Next, 100 µl of the initial CTAB-capped gold clusters was rapidly injected into the reaction mixture and hand-shaken for 5 s before being left undisturbed at room temperature. The reaction was allowed to continue for 10 min. The obtained gold nanosphere seeds were collected by centrifugation at 14,500 rpm for 30 min. After centrifugation, as much as possible of the supernatant was removed and the sediment (50 µl) was re-dispersed by the addition of 1 ml of aqueous CTAC solution (20 mM). A typical stock solution of gold nanosphere seeds has an optical density (OD) of around 1.68 at 521 nm. In the final step, aqueous solutions of CTAC (200 mM, 0.75 ml), CTAB (100 mM, 0.5 ml), AA (100 mM, 1.0 ml) and gold nanosphere seed solution (20 µl) were mixed with 0.75 ml of water in a 20 ml glass vial, followed by dropwise addition of aqueous $HAuCl_4$ solution (0.5 mM, 1 ml for small tetrahedra, 0.5 mM, 3 ml for medium-sized tetrahedra and 0.4 mM, 9 ml for large tetrahedra; Supplementary Table 1) using a syringe pump at an injection rate of 0.5 ml h^{-1}. The reaction was allowed to proceed at 27 °C for 10 min after completion of the injection. The reaction mixture was then transferred to a 15 ml centrifuge tube (Corning) and centrifuged once (8,000 rpm, 10 min for small tetrahedra, 7,000 rpm, 10 min for medium-sized tetrahedra and 6,000 rpm, 10 min for large tetrahedra) to remove unreacted reagents. After centrifugation as much as possible of the supernatant was removed and the sediment (50 µl) was re-dispersed by the addition of 1 ml, 20 mM CTAB into the centrifuge tube. Small tetrahedra were further used for assembly without purification, whereas medium-sized and large tetrahedra underwent further purification before use, as detailed below.

Purification of medium-sized tetrahedra

Medium-sized gold tetrahedra underwent two rounds of purification to remove small gold polyhedral particles and large plate-like impurities by depletion attraction-induced aggregation in a concentrated CTAC solution[51]. Specifically, the as-synthesized tetrahedra solution (1 ml) was mixed with an aqueous solution of CTAC (0.225 ml, 1 M) in a 15 ml centrifuge tube (final CTAC concentration of 184 mM). The solution was left undisturbed overnight so that the tetrahedra and large plate-like impurities sedimented as black solids by depletion attraction while small gold spherical particles remained dispersed in the top solution (light purple). Next, all of the upper solution was removed from the centrifuge tube and the remaining solid was re-dispersed with 1 ml of water. The solution underwent the second round of purification to remove large plate-like impurities by the addition of CTAC solution (0.15 ml, 1 M) into the centrifuge tube (final CTAC concentration of 130 mM). The solution was left undisturbed for 24 h, then 1 ml of the dark blue upper solution containing purified tetrahedra was collected in a fresh 1.5 ml centrifuge tube. The collected solution was then centrifuged at 7,000 rpm for 5 min. After centrifugation, 0.98 ml of the supernatant was removed and mixed with 0.88 ml of water and an aqueous solution of CTAB (0.1 ml, 200 mM), to reach a final CTAB concentration of 20 mM. Successful purification was indicated by a single peak of the ultraviolet–visible (UV–vis) spectrum at the maximum extinction wavelength (λ_{max}) of around 613 nm (Supplementary Fig. 1). Multiple batches of tetrahedra were prepared following the same synthesis and purification procedures, and particles with similar UV–vis spectra and sizes were combined as the stock solution, which were stored and used within 3 months. A typical stock solution has an OD of about 8.8 at 613 nm.

Purification of large tetrahedra

Large gold tetrahedra underwent a purification process similar to that detailed in the previous section. Specifically, the as-synthesized tetrahedral solution (1 ml) was first diluted with 4 ml of water and then mixed with an aqueous solution of CTAC (0.434 ml, 1 M) in a 15 ml centrifuge tube (final CTAC concentration of 80 mM). The solution was left undisturbed overnight so that the tetrahedra and large plate-like impurities sedimented as black solids by depletion attraction while the small gold polyhedral particles remained dispersed in the upper solution (light purple). Next, all of the upper solution was removed from the centrifuge tube and the remaining solid was re-dispersed with 2 ml of water. The solution underwent the second round of purification to remove the large plate-like impurities by the addition of CTAC solution (0.115 ml, 1 M) into the centrifuge tube (final CTAC concentration of 54 mM). The solution was left undisturbed for 24 h, then 2 ml of the dark blue upper solution containing purified tetrahedra was collected in a fresh 15 ml centrifuge tube. The collected solution was then centrifuged at 6,000 rpm for 5 min. After centrifugation, 0.98 ml of the supernatant was removed and mixed with 0.88 ml of water. An aliquot (0.5 µl) of solution containing tetrahedra was drop-cast onto a TEM grid and left to dry in air (Fig. 2a). The remaining solution was mixed with an aqueous solution of CTAB (0.1 ml, 200 mM) to reach a final CTAB concentration of 20 mM for storage. Successful purification was indicated by a single peak of the UV–vis spectrum at λ_{max} around 658 nm (Supplementary Fig. 1). Multiple batches of tetrahedra were prepared following the same synthesis and purification procedures, and particles of similar UV–vis spectra and sizes were combined as the stock solution, which was then stored and used within 3 months. A typical stock solution has an OD of about 8.6 at 658 nm.

Self-assembly of tetrahedral NPs

For the self-assembly of tetrahedra, 50 µl of NP stock solution was centrifuged in a 1.5 ml centrifuge tube at 6,000 rpm for 5 min. After centrifugation, 45 µl of the supernatant was removed and the remaining sediment re-dispersed with 45 µl of water. This freshly prepared solution was then placed in a fresh 1.5 ml centrifuge tube and mixed with aqueous solutions of Rhodamine 6G or NaCl and thiol solution (details given in Supplementary Table 2). The mixed solution was vortexed for 10 s before being left overnight on a shaker at 400 rpm. As shown in Supplementary Fig. 27, a parafilm was cut to a size of 4 × 4 inches and

placed on top of a TechniCloth (TX 609, Texwipe). The cover of a small Petri dish (60 × 15 mm^2; Fisherbrand) filled with water was placed on the parafilm. A small Si wafer (1 × 1 cm^2) was first cleaned with acetone, isopropanol and water, then 2 µl of the thoroughly mixed NP solution was drop-cast on the Si wafer placed next to the Petri dish. Typically four to six droplets were cast on the same wafer for the assembly. Immediately after drop-casting, the Si wafer and Petri dish were covered by a large Petri dish (100 × 15 mm^2; VWR). The large Petri dish was gently pressed down to ensure sealing with the parafilm underneath, to maintain a humid environment (humidity 75–80%). A typical optimal drying process requires 6–8 h at a temperature of 68–71 °F (Supplementary Fig. 8).

UV–vis, zeta potential measurements and TEM and SEM characterization

UV–vis spectra of the tetrahedra and separated impurities were measured using a Scinco S-4100 PDA spectrophotometer with a quartz cuvette (path length, 1 cm; VWR). The zeta potential of tetrahedral solution was measured using a Zetasizer Nano (Malvern). A JEOL 2100 Cryo TEM with a LaB_6 emitter at 200 kV was used for characterization of the size and shape of the tetrahedra. A Hitachi S4800 High-Resolution SEM was used for characterization of the size and shape of the tetrahedra and the structures of self-assemblies.

Interaction calculations

A coarse-grained model was constructed to calculate detailed interactions among tetrahedra. Ligand-coated tetrahedra were discretized as a mesh of beads with mesh spacing of Δ_a = 0.667 nm for gold particles and Δ_b = 1 nm for ligands. Beads were treated as point-like particles, and interactions between two tetrahedra with different offset configurations were calculated by summing all pairwise interactions between all beads of the two tetrahedra. Total interaction was calculated by summing pairwise interaction between one pair of interlayer and two pairs of intralayer tetrahedra. Additional model and calculation details are provided in Supplementary Note 3.

OPD parameter calculations

We calculated the OPD parameters of seven pinwheel structures with different corner offsets (Δ = −0.75, −0.50, −0.25, 0, 0.25, 0.50 and 0.75). The models were constructed with six medium-sized tetrahedra, and 30 coordinates were extracted from the structure to represent their centre of masses and corners. To facilitate recognition of the top and bottom layers of the structure by substrate as an experimental set-up, we placed four additional points on the same plane. The gyration tensor for OPD parameters was calculated using MATLAB codes. The measures indicate that pinwheel structures on the substrate are true geometrical enantiomers whereas their free-standing structures are achiral with inversion symmetry. Additional model and calculation details are provided in Supplementary Note 4.

FDTD simulations

Electromagnetic simulations of extinction, CD, *E*-field and magnetic field maps around the tetrahedron assemblies were calculated using the commercial software package Lumerical FDTD Solutions, 2020 R2. The models of tetrahedron assemblies were created with Autodesk 3ds Max software based on SEM and TEM images and then imported into FDTD. The assemblies were placed in the *x*–*y* plane under irradiation by circularly polarized light (CPL) from the forward direction of the *z* axis. The irradiated CPL was composed of two total-field scattered-field sources with the same *k*-vector but with a phase difference of −90° for LCP and +90° for RCP. Two analysis groups consisting of a box of power monitors were used to calculate absorption and scattering intensity, respectively, then extinction was calculated as the sum of absorption and scattering. The CD was calculated as the extinction difference under LCP and RCP, and the *g*-factor was calculated as CD normalized by average extinction under LCP and RCP. *E*-field and magnetic field maps were collected by the frequency profile monitors placed at different *z* heights—that is, top, middle and bottom planes of the models (Supplementary Fig. 11). For comparison with the *E*-field maps experimentally collected using PINEM, simulated *E*-field maps were summed using maps obtained at different *z* heights. Considering the angle effect of models on plasmonic chiroptical activity, domains of three-particle monolayer and four-, six- and 72-particle bilayers with variable Δ (Supplementary Figs. 17 and 18) were rotated in the *x*–*y* plane from 0 to 350° at intervals of 10°; final extinction, CD and *g*-factor spectra were averaged from results obtained at all angles. Other models were computed with the same angle consistent with PINEM characterizations. The excitation wavelengths for extinction and CD spectra were set in the range 300–1,200 nm, while *E*-field and magnetic field maps were excited according to peak positions in extinction and CD spectra (Supplementary Figs. 11–19). The refractive index for gold was obtained from the Johnson and Christy database, and that for backgrounds was 1.0003 to simulate the air environment.

PINEM characterization

Medium-sized tetrahedral NPs were incubated overnight with varying amounts of Rhodamine 6G molecules (conditions shown in Supplementary Table 2). Silicon nitride TEM chips (5 nm thickness; SIMPore) were first treated with oxygen plasma (Harrick Plasma Cleaner, no. PDC-32G) at low radio frequency (RF) with power of 7 W for 60 s, then 0.3 µl of liquid was added to the window area and left to dry slowly in a Petri dish. The location of the droplet was chosen to ensure that the final dried sample location would cross the window area for UEM measurement. PINEM experiments were conducted on a UEM platform at the Center for Nanoscale Materials, Argonne National Laboratory. The UEM is based on a JEOL 2100 Plus TEM, with modifications for optical access to the gun and specimen region. The UEM was operated at 200 kV voltage for the work presented here. The femtosecond laser output a fundamental wavelength of 1,030 nm with a pulse duration of 280 fs, which was split into two beams. One laser beam was frequency-quadrupled to 258 nm and was guided to the microscope cathode to produce the pulsed electron packets as probe electrons; the second laser beam was used to drive an optical parametric amplifier (OPA). The OPA output a 670 nm laser beam with a shorter pulse duration of 50 fs, which was directed to the column to photo-excite the sample as the pump beam. Pump beam polarizations of LCP or RCP were realized by a quarter waveplate in the pump beam path. After excitation of the plasmon mode of the bilayer assembly by the pump beam, an evanescent electromagnetic field developed and probe electrons travelling through the evanescent field could be scattered inelastically by gain or loss of one or more quanta of photon energies. The PINEM images herein were obtained by collecting those electrons that gained energy using an energy filter to present the plasmonic field distributions of the bilayer assembly.

Liquid-phase TEM imaging

Liquid-phase TEM imaging was performed on a Hitachi 9500 TEM with a LaB_6 emitter at 200 kV and a liquid-flow TEM holder (Hummingbird Scientific). TEM videos were captured by a Gatan Orius fibre-optically coupled CCD camera with an exposure time of 0.1 s at 10 fps. For liquid-phase TEM imaging of gold tetrahedral NP assembly, 2 µl of thiol-modified gold tetrahedral NPs (solution preparation given in Supplementary Note 6) was mixed with 0.8 µl of 150 mM PBS, pH 8.0. Next, 0.1 µl of this solution was placed on the bottom SiN_x chip (window: 50 µm × 200 µm × 50 nm, 250 nm spacer; Hummingbird Scientific) and assembled with the upper SiN_x chip (window: 30 µm × 650 µm × 50 nm; Hummingbird Scientific). Both chips were pretreated with oxygen plasma (Harrick Plasma Cleaner, no. PDC-23G) at low RF with power of 7 W for 27 s. Following chip assembly, we flowed 50 mM PBS through the liquid-flow holder for 2 h at 5 µl min^{-1} to ensure that the whole liquid chamber had reached this PBS concentration. Water was then flowed at 5 µl min^{-1} for 30 min to disassemble the clustered gold tetrahedral

NPs into individual NPs. The assembly of tetrahedral NPs was triggered by flowing 20 mM PBS solution at 5 μl min^{-1} for 30 min, and imaged at a dose rate of 11.0 e^{-} $Å^{-2}$ s^{-1}.

Data availability

The datasets generated during and/or analysed during the current study are available in the Illinois Data Bank (https://doi.org/10.13012/B2IDB-0873473_V1).

Code availability

The codes used for data analysis during the current study are available from GitHub (https://github.com/chenlabUIUC/TetrahedraProject_2022).

49. Zheng, Y. et al. Seed-mediated synthesis of gold tetrahedra in high purity and with tunable, well-controlled sizes. *Chem. Asian J.* **9**, 2635–2640 (2014).
50. Zhou, S. et al. Enabling complete ligand exchange on the surface of gold nanocrystals through the deposition and then etching of silver. *J. Am. Chem. Soc.* **140**, 11898–11901 (2018).
51. Kim, A. et al. Tip-patched nanoprisms from formation of ligand islands. *J. Am. Chem. Soc.* **141**, 11796–11800 (2019).

Acknowledgements Experiments were carried out in part in the Materials Research Laboratory (MRL) Central Research Facilities, University of Illinois. We thank J. Spear and H. Zhou (MRL) for assistance with SEM measurements. We are grateful to D. Vecchio for participation in the calculation of *CI*. This research was supported by the Office of Naval Research (no. MURI N00014-20-1-2479). S.Z. and Q.C. thank the Alfred Sloan Foundation for support via the Sloan fellowship. We also thank the Center for Nanoscale Materials, a US Department of Energy Office of Science User Facility, supported by the US Department of Energy, Office of Basic Energy Sciences, under contract no. DE-AC02-06CH11357. N.A.K., J. Lu and J.-Y.K. thank the Vannevar Bush DoD Fellowship (to N.A.K.) entitled 'Engineered Chiral Ceramics' (no. ONR N000141812876). FDTD simulations and OPD calculations were supported by NSF (no. 1463474, entitled 'Energy- and Cost-Efficient Manufacturing Employing Nanoparticles'). Research by A.T. was supported by the US Department of Energy (US DoE), Office of Basic Energy Sciences, Division of Materials Sciences and Engineering. Ames National Laboratory is operated for the US DoE by Iowa State University under contract DE-AC02-07CH11358.

Author contributions S.Z., J. Li, J. Lu and Q.C. designed the experiments. S.Z. and J. Li performed the experiments and data analysis. J. Li performed interaction calculations. J. Lu and N.A.K. performed FDTD simulations and analysed simulation data. H.L., Z.D.H., T.E.G. and I.A. performed PINEM experiments. J-Y.K. performed OPD calculations. S.Z. and A.K. performed tetrahedron purification. L.Y. developed protocols for image analysis and particle tracking. C.L., C.Q. and J. Li performed liquid-phase TEM experiments. N.A.K. built the GT model of the superlattices and calculated the *CI* values of the superlattices. W.C. contributed to property discussions. X.L. and A.T. contributed to geometric calculation and analysis. K.S. contributed to Maxwell lattice construction and discussion. All authors contributed to the writing of the paper. Q.C. and N.A.K. supervised the work.

Competing interests The authors declare no competing interests.

Additional information

Supplementary information The online version contains supplementary material available at https://doi.org/10.1038/s41586-022-05384-8.

Correspondence and requests for materials should be addressed to Nicholas A. Kotov or Qian Chen.

Peer review information *Nature* thanks Ou Chen, Andrei Petukhov and the other, anonymous, reviewer(s) for their contribution to the peer review of this work. Peer reviewer reports are available.